3D Bragg coherent diffraction imaging of extended nanowires: defect formation in highly strained InGaAs quantum wells

Megan O. Hill, †, Paul Schmiedeke, †, Chunyi Huang, † Siddharth Maddali, Xiaobing Hu, †, Stephan O. Hruszkewycz, Jonathan J. Finley, † Gregor Koblmüller, *, † and Lincoln J. Lauhon*, †

†Department of Materials Science and Engineering, Northwestern University, Evanston, IL 60208, United States

‡Walter Schottky Institute and Physics Department, Technical University of Munich, Garching, 85748, Germany

¶Materials Science Division, Argonne National Laboratory, Argonne, IL 60439, United States

§The NUANCE Center, Northwestern University, Evanston, IL 60208, United States

||Contributed equally to this work

E-mail: gregor.koblmueller@wsi.tum.de; lauhon@northwestern.edu

Abstract

InGaAs quantum wells embedded in GaAs nanowires can serve as compact near-infrared emitters for direct integration onto Si complementary metal-oxide semiconductor technology. While the core-shell geometry in principle allows for a greater tuning of composition and emission, especially farther into the infrared, the practical limits of elastic strain accommodation in quantum wells on multi-faceted nanowires have not been established. One barrier to progress

is the difficulty of directly comparing the emission characteristics and the precise microstructure of a single nanowire. Here we report an approach to correlating quantum well morphology, strain, defects, and emission to understand the limits of elastic strain accommodation in nanowire quantum wells unique to their geometry. The primary methodological advance is in the realization of fully 3D Bragg coherent diffraction imaging (BCDI) of intact quantum wells on vertically oriented epitaxial nanowires, which enables direct correlation with single-nanowire photoluminescence. By growing In_{0.2}Ga_{0.8}As quantum wells of distinct thicknesses on different facets of the same nanowire, we identified the critical thickness at which defects are nucleated. Correlation with traditional transmission electron microscopy analysis confirms that BCDI can image the extended structure of defects. Finite element simulations of electron and hole states explain the emission characteristics arising from strained and partially relaxed regions. This novel application of 3D strain and microstructure imaging to intact nanowire core-shell structures, with application relevant dimensions, is a significant advance towards predictive models that enable the design of new compact infrared emitters.

Keywords

Bragg coherent diffraction imaging (BCDI), defects, nanowires, quantum well, photoluminescence, III-V semiconductors

Core-shell nanowire (NW) heterostructures are of great interest for device applications including light emitting diodes, lasers, photo detectors, solar cells and high-mobility transistors. ^{1–6} The extremely small NW footprint enables the integration of lattice mismatched materials, such as III-Vs on complementary metal-oxide semiconductor (CMOS) compatible Si substrates, without degrading the NW material, ⁷ and the growth of quantum wells (QWs) on vertical NWs decouples the active region of devices from the influence of the substrate. Furthermore, the core-shell geometry

allows for high levels of strain accommodation in pseudomorphically grown heterostructures,⁸ as shown in various materials systems including InGaAs-GaAs,⁹ InAs-InP¹⁰ and Si-Ge.¹¹ While the enhanced strain engineering in NW heterostructures creates new opportunities for tuning materials properties and device, performance ^{12–14} it is more challenging to understand and control strain in the complex NW geometry compared to thin film heterostructures.

Theory and modeling have played an important role in understanding and predicting the onset of defect formation in core-shell heterostructures. ^{15–17} One key finding is that the theoretical critical layer thickness in the shell of NWs is increased compared to planar structures for two reasons. First, the coaxial geometry of NWs enables enhanced strain relaxation parallel to the growth interface, which increases in area with time. Second, the core diameter can be comparable to shell thickness, leading to strain accommodation primarily in the core instead of the shell. ¹⁶ Indeed, strains of over 3% without defect formation have been observed for numerous NW core-shell systems including Si-Ge, ¹¹ GaAs-GaP, ¹⁸ GaAs-InGaAs, and GaAs-InAlAs. ¹⁹ A reduction in the GaAs bandgap up to 600 meV (40%) has been observed, demonstrating the extreme tunability of III-V structures in the core-shell NW geometry. ^{18,19} However, theoretical work has been primarily limited to simpler NW structures such as cylindrical NW geometries with single shells. In this context, experimental studies that are sensitive to both strain and low densities of defects are critically important, and methods that can study intact single NW heterostructures are particularly valuable.

At the ensemble level, synchrotron-based grazing-incidence X-ray diffraction (GIXD) has been used to analyze the coherency limit in intact core-shell III-V NWs. With the aid of structural modeling, authors were able to propose a phase diagram defining the range of phosphorus content and shell thickness required for pseudomorphic growth. ²⁰ Micro-Raman spectroscopy can measure the average strain in single core-shell NWs and, due to the relative ease of measurement, readily correlate single-NW properties with the characteristics of ensembles. ^{18,19} For individual NWs, geometric phase analysis (GPA) of transmission electron microscopy (TEM) images can be used to reconstruct high spatial resolution strain maps in cross-sectional lamella. ^{21,22} In-situ TEM of small diameter Ge-Si core-shell NWs was used to determine the shell thickness at which defects

form and describe the relaxation mechanisms. ¹¹ Using TEM Moiré patterns Popovitz-Biro et al., identified defects and measured lattice misfit in InAs-GaAs NWs with a field of view larger than 300 nm. ²³ While electron microscopy provides the necessary resolution for single nanostructure and single defect characterization, the requirement of electron transparency precludes the direct analysis of intact core-shell NWs with larger diameters that are optimal for photonic applications. Furthermore, the milling of NW heterostructures can modify the strain state and complicate comparison with correlated property measurements.

Recent advances in coherent X-ray sources and information retrieval methods create new opportunities for the non-destructive imaging of single NW heterostructures that are too large for direct analysis by TEM. For example, nano-focused X-ray diffraction and coherent diffraction imaging have allowed for 2D strain mapping in core-shell NWs with resolution as high as 5 nm. 24-27 The 2D strain maps can be compared with simulations using 3D finite element modeling (FEM) to interpret the strain and defect structure of thick core-shell III-V NWs. ^{28–34} However, given that defects interrupt the translational symmetry of core-shell NWs along the NW axis, 3D approaches to high resolution strain mapping are needed. Bragg coherent diffraction imaging (BCDI) is a particularly promising approach to 3D imaging due to its high spatial resolution and strain sensitivity. 35,36 BCDI measurements involve oversampling diffraction patterns of a single nanocrystal illuminated under a microfocused coherent X-ray source. From the diffraction patterns, spatially resolved phase fields are retrieved to produce 3D reconstructions of lattice displacement within the crystal along the direction of the selected Bragg peak. Multiple Bragg peaks can be acquired on a single object to create a 3D reconstruction of the full strain tensor. ³⁷ 3D BCDI requires that the object is smaller than the coherent beam (~0.5-2 µm); NWs have not been extensively studied using BCDI in part because they do not meet this criterion. To date, 3D BCDI reconstructions of NWs have been limited to out-of-plane strain, i.e. mapping the spacing between planes along the NW growth direction. ^{29,35,38–43} An out-of-plane condition, such as (111) in zincblende (ZB) (as labeled in Figure 1(a)) is usually chosen because it is a symmetric scattering condition ($\theta = 2\theta$) and is easily accessible for NWs in the vertical geometry. While out-of-plane strain measurements can probe variations along the NW length, they are not ideal for investigating radial NW heterostructures with complex variations in in-plane strain (NW radial direction), as is the case for core-shell heterostructures. BCDI investigations of in-plane strain in NWs have been reported, but to date have been limited to 2D projections along the NW length, requiring full translational symmetry. ^{27,39,43,44}

Here we report the 3D imaging of strain and defect formation using BCDI in advanced radial core-multishell heterostructures to probe the coherency limit in the technologically relevant GaAs-InGaAs material system. InGaAs QWs of distinct thicknesses, from 2 to 20 nm, were grown on arrays of NWs by selectively exposing different facets during molecular beam epitaxy. Patterning the arrays at an appropriate pitch enabled correlated studies of BCDI and micro-photoluminescence (µ-PL) on individual NWs. For the first time in NWs, 3D maps of in-plane and out-of-plane strain components were obtained via BCDI. The resolution approaches ~5 nm as defined by the extent of scattering in reciprocal space, giving a voxel size, and therefore maximum resolution, of 4.9 nm. Additionally knife-edge measurements were performed across multiple line cuts from NW-2 to estimate a real space resolution of 6.5 ± 1.7 nm The onset of plastic relaxation was observed in the 20 nm QWs and the position of the associated dislocation cores was mapped in 3D. By complementing BCDI and μ-PL analysis with HRTEM of select NWs, the emission features in μ-PL could be assigned to specific QWs and correlated with the 3D strain state. Furthermore, we reported that crystallographic twinning along the NW growth axis can lead to different Bragg conditions for sub-segments of the NW, demonstrating a new approach to BCDI reconstruction even in the absence of full-field illumination. The powerful methodology reported here can be expanded to other NW core-shell systems of interest for e.g. nanolasers and microLEDs to establish coherency limits for radial QWs, and will provide essential inputs to new theories of core-shell growth that support the design of these advanced non-planar heterostructures for targeted applications.

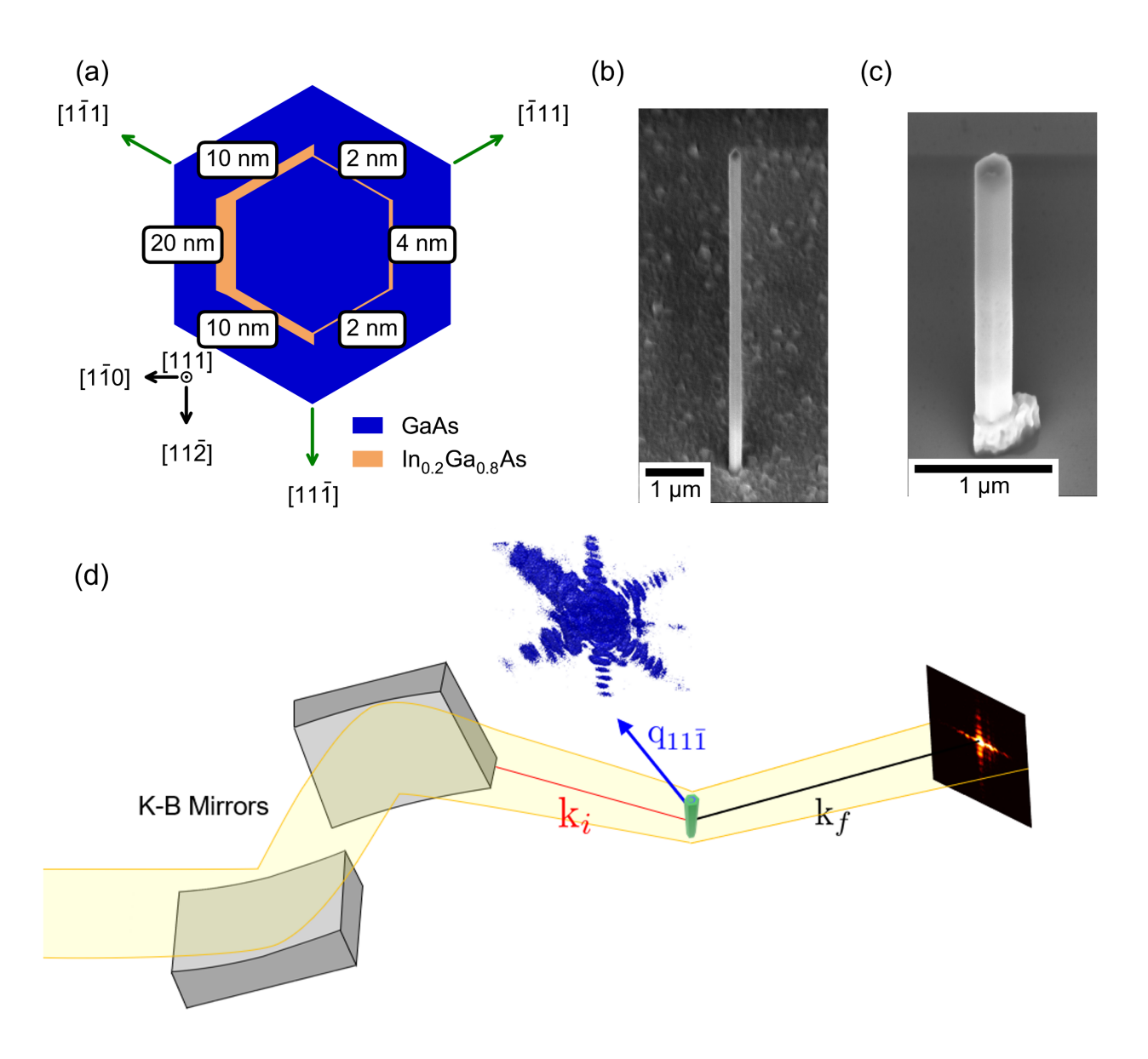


Figure 1: (a) Schematic cross-section of the NW heterostructure with relevant crystal directions. The green arrows indicate an additional out of plane component. (b) 45° tilted-view SEM image of an exemplary NW after growth on Si(111) and (c) a different NW after post-growth processing. (d) Schematic of BCDI experiment at the $(11\overline{1})$ condition. A set of Kirkpatrick–Baez mirrors were used to focus the coherent X-rays onto the NW along k_i diffracting along k_f onto a 2D CCD detector. The q-vector points to the location of the reciprocal space peak. The 3D diffraction pattern for NW-1 is shown in blue.

Experimental design

The NWs were grown using molecular beam epitaxy, as described in detail in the supplementary information (S.I.). First, vertical GaAs NWs were grown using the self-catalyzed vapor-liquidsolid (VLS) growth mode. Under our growth conditions, the NWs crystallize mostly in the ZB phase with a low density of twin defects and potential wurtzite (WZ) segments along the NW axis. 45 We use digital growth without substrate rotation to intentionally define a highly asymmetric GaAs-InGaAs QW heterostructure. It consists of a thick InGaAs QW on one side of the NW with a thickness of 20 nm on the main and 10 nm on neighboring facets, and a 4 nm thin QW on the other side of the NW as shown in Figure 1(a). Previous BCDI studies have shown that if NWs are removed from their native growth substrate and placed on another, the in-plane scattering is highly sensitive to twisting and bending induced at the interface of the lying-down NW and the substrate. 46 For this reason the NWs were left in their as-grown vertical geometry. A scanning electron micrograph (SEM) of an exemplary NW from this growth is shown in Figure 1(b). Despite the asymmetric QW no bending was observed in either SEM or BCDI, possibly due to local relaxation and the short NW length. Regions of low crystal quality, such as the NW tip and the parasitic growth on the substrate surface, seen in 1(b), can all contribute to the BCDI signal. Following NW growth, these regions were therefore selectively etched using a combination of e-beam- and photo-lithography and wet etching (see S2 of the S.I.).

The employed BCDI geometry is seen in Figure 1(d), where the NW is illuminated at a low incidence angle with respect to the (111) planes to collect the primarily in-plane (11 $\overline{1}$) diffraction condition. This low incident angle required for in-plane imaging means the length of the NW must be smaller than the X-ray beam spot (typically 0.5–2 µm) in order to be fully illuminated. For this reason the ~5 µm long NWs were shortened (see S2 of the S.I.). Another NW from the same growth is shown after fabrication in Figure 1(c).

BCDI was directly performed on the post-processed NWs standing vertically on the native Si(111) substrate. This experimental design allows us to coincidentally investigate the spatial resolution capabilities of BCDI by probing QWs of various thicknesses. It also enables the immediate

correlation with μ -PL measurements, performed on the same NWs after BCDI, where we expect spectrally separated emission from the thick and thin QWs on opposing facets, allowing us to describe the emission properties with respect to different strain and confinement states. We continue to showcase these findings by combining experimental PL analysis and modelling on single NWs, as-prepared on the growth substrate.

Photoluminescence Characterization

Single NWs were excited at a temperature of 10 K using a pulsed titanium sapphire laser and detected by a spectrometer with an LN2 cooled InGaAs array photodetector. The NWs were standing on their native growth substrate, where the excitation and detection were performed from the top. Characterizing the NWs in their intact as-grown state enables the direct correlation of optical properties with NW microstructure analyzed by BCDI below. Furthermore, the growth of QWs of distinct thicknesses on each NW allows us to explore the influence of strain relaxation on PL spectra in a very controlled manner, as a given NW can exhibit spectrally separable emission from both unrelaxed and partially relaxed QWs.

Figure 2(a) shows spectra of two NWs at low pump fluence. Both NWs are from the same growth run and were subjected to identical processing. Additionally, NWs were grown 10 µm apart to prevent shadowing during shell growth. The NWs present emission features in the range of 1.2 to 1.4 eV, which clearly stems from the InGaAs QWs. Emission at the GaAs bandgap around 1.5 eV is not observed, demonstrating that the carriers excited in the GaAs shell are either collected by the QWs or recombine nonradiatively at the surface. The two NWs differ slightly in emission energy. The dominant emission is different between the two NWs. NW-1 (top) exhibits two dominant peaks at 1.25 eV and 1.3 eV and a weak signature at 1.35 eV. NW-2 (bottom) exhibits dominant emission with several sub-peaks centered around 1.35 eV and weak, broad emission between 1.25 eV and 1.3 eV. The differences in emission energies are due to a combination of differences in the local defect structure and the average In-content (see S3 of the S.I.). In order to assign specific peaks in the experimental spectrum to specific QW thicknesses, we performed scan-

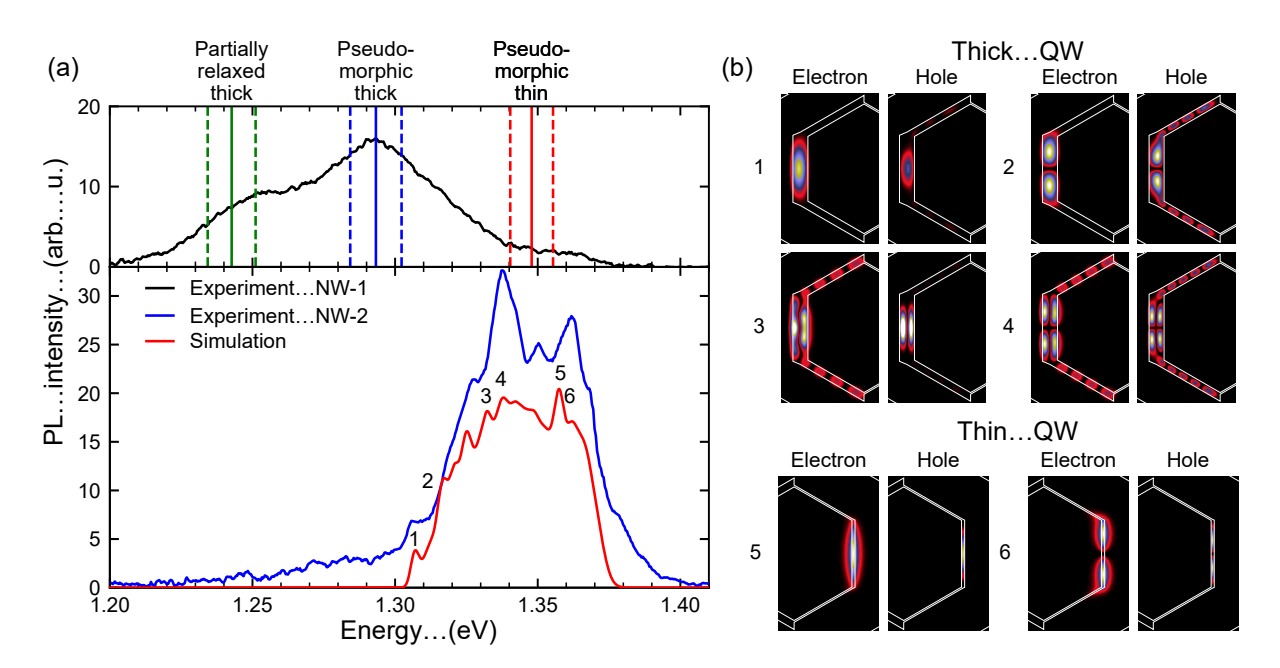


Figure 2: (a) μ -PL spectra of NW-1 (top) and NW-2 (bottom) at low pump fluence (0.18 μ J/cm²). The ground state transitions of the pseudomorphic thick QW, partially relaxed thick QW, and pseudomorphic thin QW are marked by vertical lines for an In-content of 24% on top. Dashed lines denote ± 1 % uncertainty in In-content. The red line is a simulated emission spectrum yielding excellent agreement in spectral position and relative intensity of several sub-peaks in NW-2. (b) Selected QW states, which lead to the marked sub-peaks in (a).

ning transmission electron microscopy and energy-dispersive x-ray spectroscopy (STEM-EDX) on a NW from the same sample and used the information obtained to model the QW electronic states.

For STEM-EDX, a lamella was prepared that contained a cut through the middle of the NW in $[1\overline{1}0]$ direction. Both the 20 nm and the 4 nm thick QWs were detected based on the In signal. Line scans at different positions along the NW-axis were used to estimate an In-content of $18\pm 8\,\%$ and a thickness of $19\pm 7\,$ nm for the thick QW. This value is a lower bound as the lamella may have included some finite thickness of pure GaAs either above or below the facet supporting the QW (see S.I. Figure S6(b)). Hence, the measured QW composition and thickness are consistent with expectations for the nominal In-content and QW thickness of 20 % and 20 nm, respectively. This determination was not possible for the nominally 4 nm QW due to the limited resolution of the STEM-EDX measurement. Because the growth conditions were identical for both QWs (see S9 of the S.I.), we assume that they have the same In-content and growth rate in FEM simulations.

In addition, we analyzed variations in lattice spacing between the GaAs core and the thick InGaAs QW at different positions along the NW axis using TEM (see S9 of the S.I.). We find that the [111] lattice spacing of the 20 nm QW, which is parallel to the NW growth axis, is in some regions the same for the core and shell (pseudomorphic case), 8 whereas in other regions the QW lattice spacing is up to 0.78 ± 0.14 % larger. The expected lattice mismatch between GaAs core and InGaAs QW is 1.45 % for an In-content of 20 %. Hence, we preliminarily conclude that the ~20 nm thick QW exceeds the coherency limit, leading to partial strain relaxation and modification of the PL spectra. The effects of partial strain relaxation on the μ -PL spectrum can be diverse: Firstly, they can cause the spectrum to red-shift. Secondly, the spectrum broadens due to local variations in strain and thirdly, the PL intensity decreases due to additional non-radiative recombination. $^{47-51}$ Further support for this hypothesis is provided by the BCDI analysis below.

The electronic states of the QWs were calculated using 8 band k·p theory using nextnano++,⁵² taking into account pseudomorphic strain, but neglecting Coulomb interactions (see S4 of the S.I.). We model the emission from the partially relaxed regions of the thick QW by reducing the strain by an amount consistent with the observed difference in lattice constant, leading to a red-

shift of the QW emission. We find overall best agreement of the ground state transitions with the experimentally observed emission features of NW-1 using an In-content of 24%. The bandgap of In_{0.24}Ga_{0.76}As is ~1.17 eV at 10 K, which here increases up to ~1.29 eV in the pseudomorphic and to ~1.23 eV in the partially relaxed QW due to the compressive strain. Quantum confinement causes an additional shift to higher energies of the electron and hole states. The resulting ground state transition derives from the first sub-band of the thick (20 nm) pseudomorphically strained QW with a transition energy slightly below 1.3 eV; the first transition associated with the thin (4 nm) QW is expected slightly below 1.35 eV. The reduced strain in partially relaxed regions leads to a red-shift of the thick QW's emission to approximately 1.25 eV.

Features from the thick and thin QWs can be identified in the spectrum of NW-1 and are marked in blue and red, respectively, defining the range of emission expected for the pseudomorphic QWs. The red-shift due to partial strain relaxation accounts rather well for the low energy peak of NW-1. The dashed lines show the influence of 1% variations in In-content to illustrate how small compositional variations will influence emission. Considering that we observe only partial strain relaxation of the thick QW, it is surprising that the 4 nm thin QW shows no spectrally sharp emission feature for NW1, since it should be well below the critical layer thickness. As shown later by BCDI, defects extend towards the corner between the 10 nm and 2 nm QW. It seems reasonable to assume that these can act as a nonradiative recombination channel for carriers in the 4 nm thin QW as well and suppress and broaden its emission.

Due to the pulsed excitation scheme, higher order transitions should manifest in the emission spectra as a complex sub-peak structure. Indeed, the spectrum of NW-2 clearly exhibits several sub-peaks that are sufficiently resolved to assign to distinct QWs based on two dimensional modeling of the electronic states. We calculate confinement energies and the corresponding emission spectrum resulting from the confinement by the thicknesses and widths of the QWs, noting that the facet size determines the QW width. We perform a single simulation of all QWs simultaneously, where we take into account 70 hole and 50 electron states and transitions from each electron to each hole state. To best fit the low energy side of the experimental data of this NW, we employ a

slightly reduced In-content of 22.5 %, which is well within the experimental error of the STEM-EDX measurement. Due to the numerous necessary assumptions involved in the modelling and the complexity of the microstructure, μ -PL alone is not suitable to determine the In-content with high accuracy. (see S4 of the S.I.)

Figure 2(b) shows example pairs of electron and hole states that have particularly large overlap integrals and are thus most likely to contribute peaks in the emission spectrum. The lowest energy transitions of the thick and thin QWs, shown as transition 1 and 5, respectively, are each characterized by a single maximum in their probability densities. The hole state of transition 1 is centered in the 20 nm QW but extends into the 10 nm QW. We note that the hole ground state is fully localized in the 10 nm QW because the strain locally reduces the bandgap (not shown). However, this state does not lead to an optically active transition because it does not have a large overlap with the electron ground state 1. Thus, the electronic states of the 10 nm and 20 nm QWs cannot be treated separately.

Transition 2 is associated with an additional probability density peak inside the 20 nm QW, leading to a small increase in emission energy of ~5 meV compared to transition 1. Random variations in QW size and composition along the NW axis likely prevent us from distinguishing between transitions 1 and 2; as indicated in (a), a 1 % variation in In-content leads to an energy-shift of ~8 meV. This broadening is accounted for in the simulation by a Gaussian line shape function. In addition, Coulomb effects are expected to diminish the observed peak in the experimental spectrum, ⁵³ further inhibiting the distinction between spectrally adjacent transitions.

Transitions 3 and 4 arise from the first transitions of the second sub-band of the thick QW. We observe that the energy spacing between individual QW sub-bands (transitions 1 and 3) is significantly larger (25 meV) than between states of the same sub-band (transitions 1 and 2), since the thickness of the thick QW is much smaller than the extension of the QW along the side facet. Hence, we attribute the peaks around 1.34 eV, which are the strongest in the experimental spectrum, to transitions 3 and 4. Furthermore, the experimental peak at 1.36 eV coincides with the first sub-band of the 4 nm thin QW (transitions 5 and 6).

This model only takes into account the pseudomorphic QWs and does not describe the broad low-energy emission of NW-2 between 1.25 eV and 1.3 eV, which appears at higher pump fluence (see S3 of the S.I.). We attribute this emission to the observed partial strain relaxation, which experiences strong broadening due to variations along the NW axis. Hence, we do not observe a well-defined peak but rather a long low energy tail.

To summarize, the combined PL and TEM analyses and simulations indicate that there are distinct regions of pseudomorphic and partially relaxed growth for the 20 nm QW, leading to both discrete emission features as well as broad emission bands associated with variations in defect density, composition and strain. To confirm this picture and analyze the strain state and defect structure in as-grown NWs, we pursued BCDI analysis on the same NWs as analyzed by PL.

Bragg Coherent Diffraction Imaging

BCDI measurements were performed at the 34-ID-C beamline of the Advanced Photon Source; an example scattering geometry is shown in Figure 1(d). A pair of Kirkpatrick–Baez (K-B) mirrors focused X-rays onto the vertical NW on the growth substrate, and the 9 keV X-ray beam incident along \tilde{k}_i was scattered from the NW along the final direction \tilde{k}_f onto a charge coupled device detector (CCD). Vertical and horizontal beam slits were tuned to maximize the probe size. We note that the vertical width sets the limit for full-field illumination of NWs in BCDI measurements because the NWs are longer than they are wide. 3D diffraction patterns were collected for six NWs at the $(1\bar{1}1)$ reflection, and the $(11\bar{1})$ peak was collected for five of the same NWs (see S5 of the S.I). Figure 3(a) shows an isosurface (>3 photons) of the 3D diffraction pattern for the $(11\bar{1})$ scattering of NW-1, the same NW investigated with PL. All other 3D diffraction patterns are shown in S5 of the S.I. This scattering condition probes the lattice displacement of the NW along the momentum vector direction $\tilde{q}_{I1\bar{I}}$, which points along the NW corner with a partial out-of-plane component (~33%), as shown by the green arrows in Figure 1(a). Since this scattering condition has a ~67% in-plane component, it is primarily detecting lattice displacement along the cross-section of the NW, the plane in which we expect a large compressive strain on the QW.

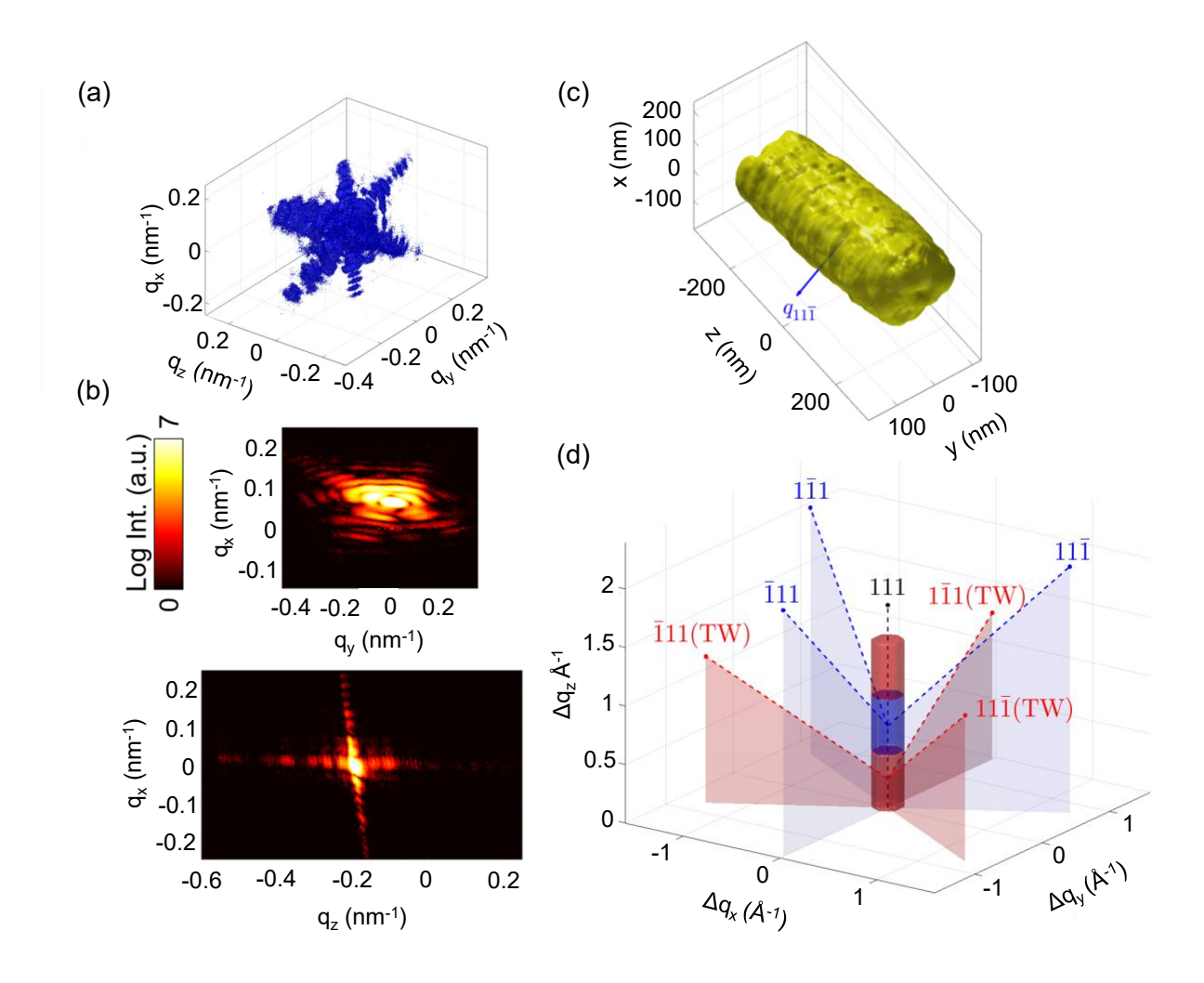


Figure 3: (a) 3D reciprocal space map (RSM) of diffraction (>3 photon count isosurface) from the $(11\bar{1})$ condition of NW-1. (b) 2D cuts of this diffraction pattern on a log scale. (c) Isosurface of the final support from the 3D reconstruction of NW-1 at $(11\bar{1})$, with the q-vector labeled. (d) Reciprocal space map of vertical $\{1\bar{1}1\}$ peaks for twinned and untwinned ZB, the twinned segment results in a 60° rotation of the $\{1\bar{1}1\}$ changing their Bragg angle. The twinned segment does not result in rotation of the (111) peak.

Figures 3(b),(c) show 2D cuts along the center of the diffraction pattern for the $(11\overline{1})$ condition for NW-1. From these cuts, eight fringing structures are visible (six in a star pattern (b) and two along \tilde{q}_z (c)). These fringes are crystal truncation rods from the six NW side facets and two NW end facets. In the diffraction pattern (b), an asymmetry in the six-fold fringes can be seen, which is expected for an asymmetric strain field from QWs of variable thickness. For this diffraction peak, 10 and 4 pixels per fringe are sampled for the six-fold and two-fold rods respectively, exceeding the

Nyquist frequency required for phase retrieval. ⁵⁴ The fringe frequency along \tilde{q}_z is ~0.012 nm⁻¹, corresponding to an object of length ~520 nm. This is unexpected because NW-1 is 1.9 µm long as measured by SEM. In fact, while a 2 µm vertical probe was desired to illuminate the entire NW, in practice, to maintain the beam coherency and flux, the vertical beam width was limited to 1.05 µm and horizontal beam width to 0.5 µm. Therefore, in this case, the 1.9 µm long NW does not fit within the coherence height of the X-ray beam, therefore there should not even be well-defined fringes along the NW vertical direction (\tilde{q}_z). However, since fringes are visible, this indicates that a crystallographically isolated segment of length ~520 nm is present within the NW. Indeed, changes in the stacking sequence along the [111] direction are common in NW growth. We hypothesize that the ~520 nm segment is bounded by deviations in stacking order, isolating its scattering from that of the rest of the NW.

To determine the structural variation leading to the reduced reconstruction, we must consider the scattering behavior of different polytypes, such as the wurtzite (WZ) and zincblende (ZB) phases, as well as ZB twin domains, which are very common in GaAs NWs. At the {111} condition, WZ has no equivalent scattering peak, so WZ regions will give zero intensity. However, at the given growth conditions, only small segments (few nms) of WZ phase are expected. Instead, the GaAs cores are expected to be primarily of ZB structure with occasional twin domains. 55 At such twin boundaries the ABC stacking changes to CBA, resulting in a change in the scattering condition. As shown in the schematic in Figure 3(d), for untwinned ZB (blue) there are three $\{11\overline{1}\}$ conditions that will scatter out of the substrate. However, upon twinning (red segment) these three $\{11\overline{1}\}\$ peaks are rotated by 60° . This schematic shows how twinned portions of the ZB NW will not satisfy the Bragg condition (if the angle is set to scatter from the untwinned ZB $\{11\overline{1}\}$). This suggests that a small number of twin defects within the NW results in the crystallographic isolation of a ~520 nm segment of otherwise untwinned ZB. In support of this hypothesis, diffraction patterns collected from the (111), see S5 of the S.I., show no fringe structure along q_z , meaning that the length of the NW indeed exceeds the size of the beam. This is expected when the NW does not fit within the beam vertically, as is true for NW-1, because the (111) condition is insensitive to rotational twins.

Since there is a fully crystallographically isolated segment of untwinned ZB within the 1.05 μ m beam, 3D reconstruction of this region is feasible. Reconstructions are obtained using a combination of iterative phase retrieval algorithms in a Python module. ⁵⁶ Details of the reconstruction are provided in the S.I. The shrinkwrap method was used during phase retrieval to update the real space support volume (every 30 iterations), evolving the object support towards the shape and size of the real space NW being reconstructed. An isosurface of the final object support from a reconstruction of NW-1 for $(11\overline{1})$ is shown in Figure 3(c), with the respective scattering vector (q) shown in blue. The reconstructed volume is ~550 nm in length, similar to what was calculated from the fringe spacing in Figure 3(b). A roughly hexagonal shape is seen in the cross-section of Figure 4 (a,b) with a diameter of ~210 nm in good agreement with the NW diameter determined by SEM.

The reconstructed phase (ϕ_{hkl}) was converted to a relative displacement field (u_{hkl}) of the hkl planes along the momentum vector (q_{hkl}) direction according to $u_{hkl} = d_{hkl} \cdot \phi_{hkl}/2\pi$, where d_{hkl} is the unstrained lattice spacing of the hkl planes. The displacement field was then converted to relative strain along q_{hkl} by taking the spatial derivative $\varepsilon_{hkl} = \delta u_{hkl}/\delta x_{hkl}$. This conversion assumes that all displacement features are a result of strain, though other deviations in lattice structure such as defects can also contribute to the calculated displacement. As such, the reconstructed "strain" maps shown may contain artifacts unrelated to strain as discussed further below.

For NW-1, cross-sectional cuts of the strain, $\varepsilon_{1\bar{1}1}$ and $\varepsilon_{11\bar{1}}$, taken at the center of the reconstructed NW, are shown in Figures 4(a) and (b) respectively. Additionally, a longitudinal cross-section of $\varepsilon_{11\bar{1}}$ is seen in 4(c), where the black dotted line is the location of the cut in (b). For reference, a schematic of the asymmetric NW structure is shown in 4(d) with $q_{11\bar{1}}$ and $q_{1\bar{1}1}$ directions marked. The q-vector is shown in purple in each strain cut, which is the direction of the strain component. Simulations of the strain were generated using finite element method (FEM) in COMSOL, as described in the S.I. The nominal NW geometry shown in Figure 1(d) was used with an In-content of 20%. Displacement fields generated in COMSOL were extrapolated onto the same grid as the reconstructed data, lowering the spatial resolution of the simulations to bet-

ter compare with the reconstructed data. Displacement was converted to strain, and the simulated strain cross-sections are shown in Figure 4(a-c) (bottom). All cross-sectional cuts are oriented in the same fashion as the schematic in 4(d).

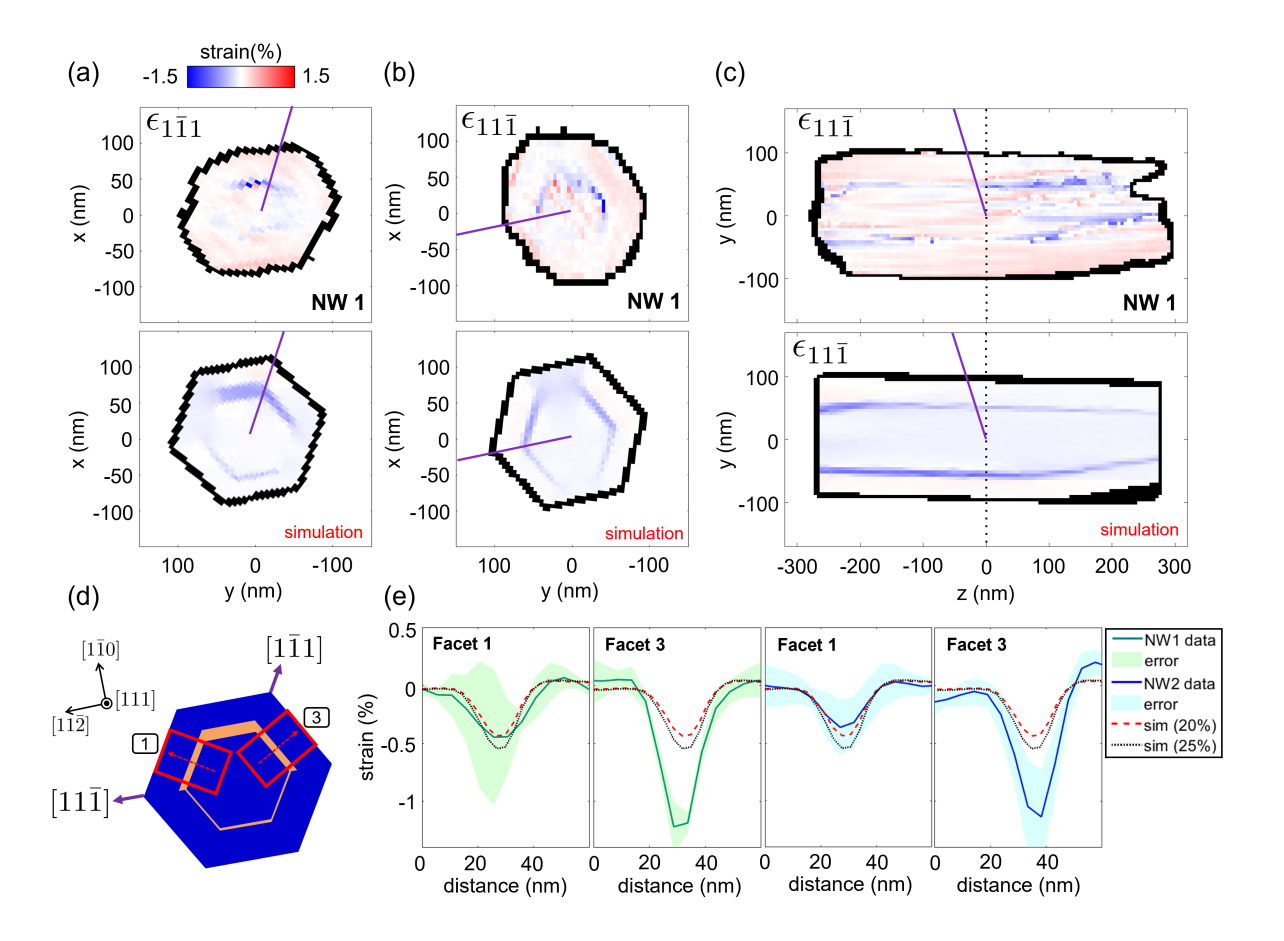


Figure 4: Experimental BCDI reconstructions and simulated strain for asymmetric QW heterostructures (a) Cross-sectional cut of the $(1\,\overline{1}\,1)$ strain of NW-1 (top) and the corresponding simulated cut (bottom). (b) Cross-sectional cut of the $(1\,1\,\overline{1})$ strain of NW-1 (top) and the corresponding simulated cut (bottom). (c) Longitudinal cross-section of the $(1\,1\,\overline{1})$ strain of NW-1 (top) and the corresponding simulated cut (bottom). Purple lines correspond to the scattering direction. The dotted black lines refer to the location of the cross sectional cuts in (b).

The strain range for (a-c) is -1.5% to 1.5%. Simulations are of QWs with 20% In-content. All cross-sections are oriented as the schematic in (d). (d) A schematic of the nominal NW heterostructure with the q-vectors for $(1\overline{1}1)$ and $(1\overline{1}1)$ shown for reference. (e) Averaged line profiles taken across the QWs labeled Facet 1 and 3 in (d), green for NW-1 and blue for NW-2. Line cuts of FEM simulations for 20% (red dashed) and 25% (black dotted) In-content are overlaid.

The simulations and experiments share important salient features. A compressive field (blue)

is observed around the thickest QW in Figure 4(a), with a lower compressive strain in the region of the bottom facet (4 nm QW). In this scattering condition $(1\overline{1}1)$, the q-vector is most sensitive to deviations in the 20 nm and 4 nm QWs because their growth facets, or interfaces with the GaAs matrix, are close to perpendicular to \tilde{q} . At the other scattering condition (111) in Figure 4(b) the cross-section shows a compressive strain around the 10 nm QWs. The longitudinal cuts in (c) show the same two bands of compressive strain due to the 10 nm QWs in the reconstruction and simulation. Again note that Figure 4(a) and (b) are derived from the same NW (NW-1), but plot different strain components; for $\varepsilon_{11\bar{1}}$ (4(b)) the strain associated with the 20 nm QW is not evident because its planes are parallel to the $q_{11\bar{1}}$ vector, whereas this strain is resolved in $\varepsilon_{1\bar{1}1}$ (4(a)). We note that discrepancies between simulation and experiment regarding strain magnitudes can arise from ambiguities in BCDI in absolute strain, from issues of signal to noise ratio, or from the presence of defects in the crystal not accounted for in FEM. The overall higher tensile strain in the NW core/outer-shell in the reconstructions, as compared to simulation, is not due to an overall tensile stress on the NW but is an effect of uncertainty in defining absolute strain. Other striations or spikes in tensile/compressive strain are likely due to limits in the reconstruction resolution or phase ramps caused by defects.

A close comparison of the simulations and reconstructions reveals a few notable differences. First, for $\varepsilon_{11\bar{1}}$ (4(b)), the strain state in the 2 nm QWs is not resolved in the experimental reconstruction, likely due to insufficient counting statistics. Further, the voxel size in the reconstruction is 4.9 nm, which determines the best possible resolution in the reconstruction (the actual resolution is determined by the extent of resolvable signal in reciprocal space); a 2 nm QW is therefore challenging to resolve. Second, also in $\varepsilon_{11\bar{1}}$, the strain appears to be larger in the right 10 nm QW than in the left, though they should be equal if the actual NW has the same symmetry as the schematic. Additionally, the longitudinal cut of $\varepsilon_{11\bar{1}}$ contains numerous high strain features that fluctuate along the NW length (Figure 4(c)). Finally, for $\varepsilon_{1\bar{1}1}$ (4(a), the peak strain in the 20 nm QW is higher than expected from the simulations.

While the strain state of the 20 nm QW is of interest, the following detailed quantitative analysis

focuses on the 10 nm QWs due to the comparatively higher quality of data collected at the (111) condition. This difference can be seen for multiple wires in in the S.I. To investigate the strain in the 10 nm QWs in more detail, line profiles of average strain were taken by summing across a 15 pixel distance (~75 nm) in the center of the QWs labeled in 4(d) as Facet 1 and Facet 3. Line cuts were averaged across five reconstructions with random starting guesses of phase and amplitudes. Profiles are shown for the 10 nm QWs in the $\varepsilon_{11\bar{1}}$ scattering condition for two NWs (NW-1 and NW-2). Red dashed and black dotted lines show the strain profiles extracted in the same fashion from the COMSOL simulation for 20% and 25% In-content, respectively. Looking first at the strain profiles of Facet 1, NW-1 and NW-2 show similar behavior and are well described by the simulated data for In-content around 25 % for NW-1 and 20 % for NW-2, corresponding well with the In-content fit to the PL data, 24 % and 22.5 % for NW-1 and NW-2 respectively. That said, the error of the line cuts from the BCDI reconstruction shows that BCDI alone cannot determine the In-content with high accuracy for such small structures. It is notable that despite the variations, features of the 10 nm QW are clearly resolvable, and even features of the 4 nm QW are evident. Increases in the exposure time or the angular range in the BCDI experiment would further constrain the reconstructions and enable reliable strain information to be extracted from few-nm QWs.

Turning to the strain profiles for Facet 3, we observe that the compressive strain within the QW is much larger (>1%) than for Facet 1, and it is larger than expected for QWs of 20% or 25% In-content. As mentioned above, the reconstructed strain maps shown in Figure 4 assume fully pseudomorphically strained QWs. However, the correlated PL and HRTEM analysis provided evidence of structural relaxation within the thicker QWs. Given the significant differences between simulation and experiment around some facets, we hypothesize that interfacial defects are making significant contributions to the representation of strain for select facets.

To understand qualitatively how defects may manifest differently than strain gradients, and therefore distinguish their contributions, it is useful to examine cross-sections of the phase (i.e. without converting to displacement or strain) for NW-2 ($\phi_{11\bar{1}}$) and NW-1 ($\phi_{11\bar{1}}$ and $\phi_{1\bar{1}1}$) in Figure 5. Figure 5(a) shows the phase in NW-2 magnified in the region around Facet 3 from (marked

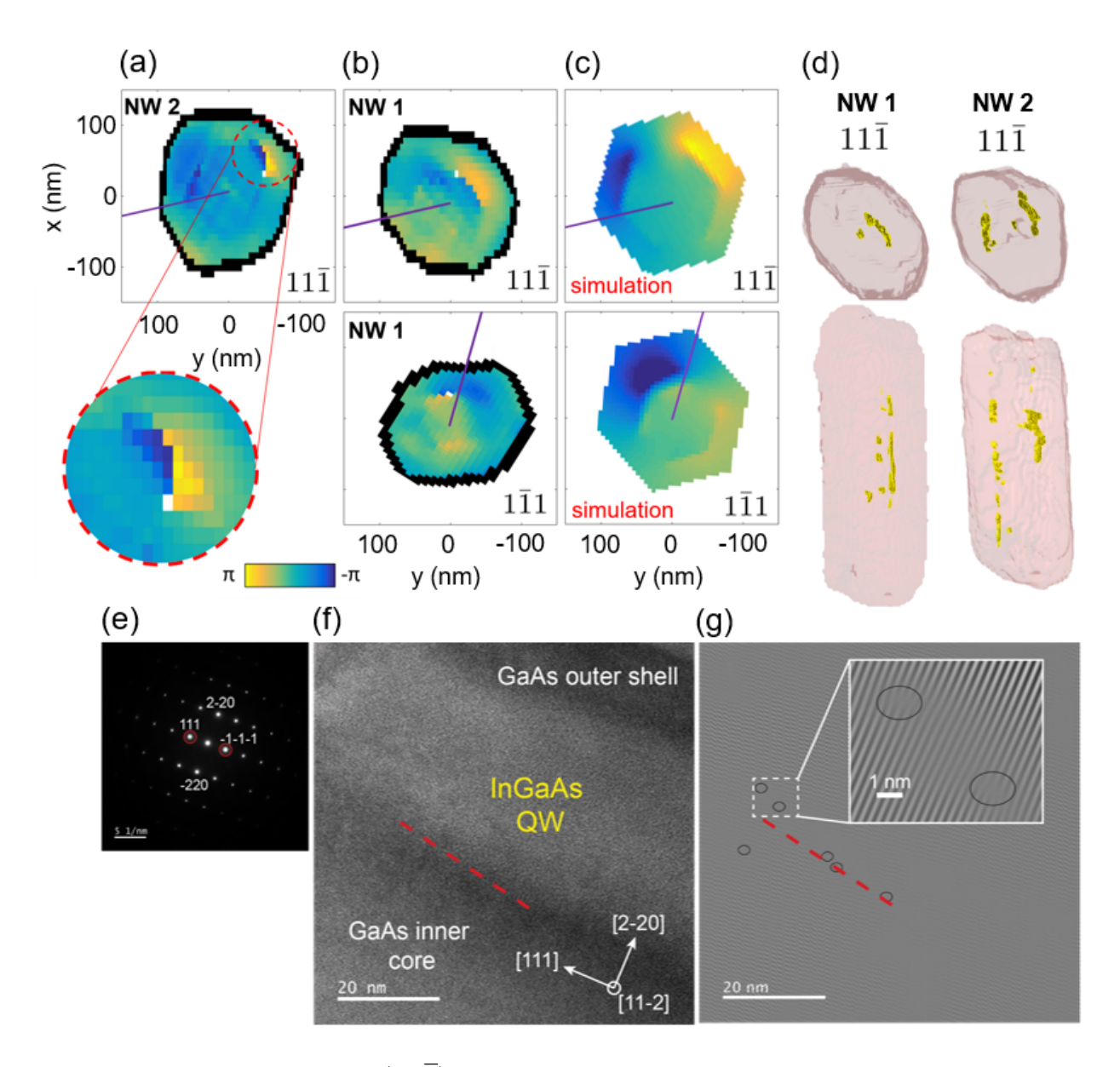


Figure 5: (a) Phase map of the $(11\overline{1})$ condition of NW-2, with the region around the 10 nm QW magnified (NW-2, Facet-3 in 4(e)). (b) Phase map for $(11\overline{1})$ and $(1\overline{1}1)$ in NW-1, top and bottom respectively. (c) Simulated $(11\overline{1})$ and $(1\overline{1}1)$ phase for 20% In QW, top and bottom respectively. Phase wraps are seen in the thickest facets for the experimental phases. The lowest amplitude pixel in each cut is marked in white, indicative of a dislocation core. (d) Mapping the 3D variations in the phase wrap for the $(11\overline{1})$ reconstruction of NW-1 and NW-2, predicting the 3D dislocation core positions following the work of Reference 57. (e) TEM diffraction pattern from the (f) TEM bright field (BF) image of a zoomed-in region of the thickest (20 nm) QW of NW-3. (g) Lattice fringes reconstructed using masks including (111) and $(\overline{111})$ reflections, which are circled in the diffraction pattern in (e). Some regions showing the presence of an extra atomic plane are marked in black ovals (a representative magnified image is shown in the inset). These regions are lined up along the NW length around the 20 nm QW.

in Figure 4(d)), which is qualitatively very different from the phase profile of the other 10 nm QW on the left side of the cross-section. Within the region outlined in red there is a clear phase wrap: from left to right the phase becomes more negative, then jumps from $-\pi$ to π across a single pixel, and then the phase moves again towards zero. Additionally, the lowest amplitude pixel (marked in white) within this cross-section is located at the core of the phase wrap. Similar features appear in NW-1 for both $\phi_{11\bar{1}}$ (Figure 5(b) top) and $\phi_{1\bar{1}1}$ (bottom) maps. Such a feature is not present in the phase maps generated from simulations of strain, $\phi_{11\bar{1}}$ and $\phi_{1\bar{1}1}$ shown in Figure 5(c).

Spatially correlated phase wraps and amplitude reductions have been observed in previous BCDI studies $^{57-60}$ and attributed to the presence of a screw or edge dislocation. 2π phase ramps occur when displacement equals a full lattice constant of the measured planes, for example of $(1\,1\,\overline{1})$ planes when measuring $q_{(1\,1\,\overline{1})}$. Phase wrap features are observed for all 6 NWs at the corners of the $10\,\mathrm{nm}$ or $20\,\mathrm{nm}$ QWs, suggesting that the coherency limit for this structure lies near an In-content of $20\,\%$.

As discussed previously, there is no general model that predicts when dislocations will form or what type of dislocations are most probable for core-shell NW heterostructures. ^{16,61,62} Qualitatively, defect formation is dependent on the core diameter, shell and barrier thicknesses, and lattice mismatch (In-content). Yan et al. ¹⁶ considered the formation of a dislocation loop and predicted critical InGaAs QW thicknesses for cylindrical NWs with similar core/barrier thickness as studied in this work (100 nm GaAs core and 50 nm GaAs barrier). Their model predicts a critical QW thickness of ~23 nm at a 20 % In-content. As a caveat, their model assumes thermodynamic equilibrium. Hence, it is assumed that dislocation formation occurs spontaneously once the reduction in elastic energy due to the reduced misfit exceeds the energy associated with that particular dislocation type. However, MBE growth takes place far from thermodynamic equilibrium, and there are activation energies associated with dislocation formation, ⁶³ implying that the observed critical QW thickness may be temperature dependent. Indeed, growth temperatures of 460°C, similar to this work, have been observed to increase the critical layer thickness of InGaAs, ⁶⁴ demonstrating the limits of a growth-parameter independent model.

Therefore, the thickest QW in this work is in a transition region only slightly below the theoretical critical layer thickness, where (partial) strain relaxation becomes increasingly likely. The PL simulations suggest that the In-content is closer to 24 % for NW-1 and 22.5 % for NW-2, making defect formation in the QWs more likely, which is further supported by the observation of partial strain relaxation via PL. Given the more complex geometry of the asymmetric QWs on an approximately hexagonal core (as opposed to models assuming a cylindrical NW shape), the influence of strain concentration on the location of defect formation should also be considered. Ultimately, it is challenging to predict, using calculations alone, the thickness and composition at which defects will form in these asymmetric structures. However, utilizing the non-destructive and three-dimensional nature of BCDI measurements, we are able to better understand the defect behavior of these heterostructures. Specifically, the BCDI reconstructions exhibit phase wraps around the 10 nm and 20 nm QWs, with minimum amplitude values at the facet corners. Since this drop in amplitude is associated with a dislocation core, BCDI reconstructions suggest that dislocations are present at the corners of the 10 nm and 20 nm facets. It is important to note that the asymmetry introduced by the distinct QW thicknesses introduces heterogeneity in the strain state that may influence the nucleation of defects. While defects form in the 10 nm QW on a facet adjacent to a 20 nm QW, this does not imply that defects will form in a symmetric 10 nm radial QW. Instead, we expect that 20 nm thickness is an upper limit for defect formation that may influence the formation of defects in the thinner adjacent QWs.

In addition to the presence of dislocations, it is important to understand the type of dislocation and the propagation of the dislocations in three-dimensions (along the NW length). Pure screw dislocations due to shell misfit in NWs are not predicted and have not been experimentally observed. Instead, either edge dislocation loops around the core or linear edge dislocations down the length of the NW are expected. Further discussion of the possible defect structures is provide in S9 of the S.I. Both of these types of edge dislocations have been observed via STEM in InAsGaAs core-shell NWs previously. To better understand the 3D behavior of the dislocations using BCDI, a min-max algorithm for tracking the presumed dislocation core was utilized, as described

in Reference 57. The algorithm calculates local minimum differentials in phase, and the pixels with differential values approaching the maximum (2π) are most likely situated around the dislocation core. A differential value of $4/3 \pi$ is plotted as an isosurface in yellow in Figure 5(d) for the (111) scattering condition in NW-1 and NW-2. This differential cut off, which is the same as differential value used in Reference 57, produces isosurfaces that extend along the growth axis. The isosurface segments are found at the corner connecting the 10 nm and 20 nm QWs on the right side, and to a lesser extent between the 10 nm and 20 nm QW on the left side. For NW-2, 5(d), isosurface cores are seen at the corners of both 10 nm QWs and the 20 nm QW. For both NWs, the dislocation cores predicted by the min-max calculation lie primarily along the length of the NW, which points to the presence of linear edge dislocations rather than loops. However, the dislocation cores are not fully continuous and do not extend along the entire NW length. This may be due to the limited experimental resolution, but it is also possible that defects are not present along the entire NW length, as already inferred from the μ-PL measurements of NW-2. The differences in PL emission energy between NW-1 and NW-2 was attributed to differences in the relative proportion of partially relaxed and pseudomorphic regions. Although BCDI studies observed comparable defects in selected segments of each NWs, μ -PL is generated by the full length of the nanowire, and preferentially in regions with fewer defects.

To confirm the presence and further investigate the nature of dislocations along the NW length, high-resolution transmission electron microscopy (TEM) was performed. A lamella, prepared by focused ion beam (FIB), was cut from a third NW from the same growth (NW-7). The bottom segment of the longitudinal cross section was captured with negligible ion-beam damage. The region around the 20 nm QW along a $\begin{bmatrix} 1 & 1 & 2 \end{bmatrix}$ zone axis is seen in Figure 5(f), as confirmed by the diffraction pattern in 5(e). To display the misfit dislocations, the lattice fringes image is reconstructed from the (111) and $(\overline{111})$ reflections (circled in Figure 5(e)) is shown in Figure 5(g). Regions with extra atomic planes, corresponding to dislocation cores, are circled in black. Dislocation dipoles are present in some regions, whereas in other regions single dislocations reside around the interface between GaAs core and InGaAs QW (along the red dashed line). Both types of dislocation give

rise to local strain variation and partial relaxation. Note that in this longitudinal projection, the corner connecting the 10 nm and 20 nm QWs overlaps with the interface between the GaAs and the 20 nm QW (see S6 of the S.I.). This is the same region where phase wraps occur in the BCDI reconstructions for NW-1 and NW-2. While the type of defect (direction of the edge dislocation) cannot be determined from this lamella, we are able to confirm that the phase wraps in BCDI are indeed the result of dislocation cores extending along the length of the NW.

Conclusions

This work demonstrated a novel integrated experimental approach to determine the critical thickness limit of NW QWs. Digital shell growth was used to fabricate asymmetric QWs by design, allowing for concurrent characterization of multiple QW thicknesses in a single device. Via finite element modeling, μ -PL spectra were directly correlated with QWs on single NWs reconstructed with BCDI, which enabled us to probe the strain state of intact buried nanostructures. Additionally, BCDI was able to identify the location of defects within the NWs, as confirmed by TEM. This powerful combination of growth, μ -PL, and BCDI provide a general methodology to explore the coherency limits of core-shell NW heterostructures in additional materials systems, such as the III-nitrides. Such studies would inform the development of a more general model of defect formation in NWs and underpin device design for emerging technologies such as μ -LEDs . While in this work only six NWs were reconstructed, straightforward modifications could allow for 50-100 NWs to be measured and reconstructed during a typical experimental run (see S5 of the S.I.), enabling for more comprehensive study of coherency limits in multi-shell nanowires.

We also reported the presence of ZB twinning, common to III-V NWs, which leads to the crystallographic isolation of segments of the long core-shell NWs, enabled reconstruction by BCDI methods even in the absence of full field illumination. The positioning of low-density rotational twins made possible the 3D reconstruction of subsections of NWs that traditionally could not be reconstructed, as they did not fit within the coherent beam spot. As it is possible to control twin formation in III-V NWs, 65 we propose that growth conditions could be intentionally designed to

isolate select portions of NWs for BCDI analysis without having to limit the NW length during growth or modify the NW structure in post-growth processing. Finally, BCDI was used, for the first time, to produce 3D in-plane strain (NW radial direction) reconstructions of NWs, enabling the mapping of dislocations along the NW length. It is notable that BCDI is able to image strain associated with features down to ~4 nm, even though the reconstructed pixel size in the crosssection was limited to 4.9 nm. The resolution of this measurement could be additionally improved with higher counting statistics or use of a higher brilliance X-ray source, which would allow for phase reconstructions of higher spatial resolution and reduced error. In general, core multi-shell NW heterostructures pose a unique opportunity to tune emission energies beyond what is possible with equivalent thin films, while minimizing defects. Indeed, defect formation could be prevented not only by controlling composition and QW thickness, but even by modifying the curvature of the hexagonal facets.⁶⁶ However, this opportunity comes with an additional challenge: determining defect coherency limits in complex 3D heterostructures. By broadening the applicability of BCDI to intact extended NW heterostructures, we believe that coherency limits can be better determined for other core-shell NW systems, providing improved input for growth and device optimization of these technologically relevant non-planar heterostructures.

Methods

Nanowire growth and processing

The nanowires (NW) are grown site-selectively by solid source molecular beam epitaxy (MBE) on Si (111) substrates with a pitch of 10 µm to prevent shadowing effects from neighboring NWs. The GaAs NW core is grown using the self-catalyzed vapor-liquid-solid (VLS) growth mechanism at a substrate temperature of 650 °C. The radial growth of the InGaAs QWs is performed as a digital alloy on the different facets at 420 °C to create intentionally asymmetric QW thicknesses. In this scheme, a single facet of the NW is rotated to face the In, As, Ga, and As cells sequentially, growing 0.289 nm layers until the QW reaches 4 nm or 20 nm (for the thin or thick facets). After

the QW growth is finished, a 50 nm thick GaAs cap layer is grown on the NW shell. More details on NW growth can be found in S1 of the S.I.

To enable BDCI measurements, the nanowires must be fully isolated from materials that diffract at the same Bragg condition. At the low temperatures needed to grow high In-content InGaAs QWs $(420\,^{\circ}\text{C})$ in MBE, 67 a parasitic polycrystalline layer grows on the SiO2 mask layer. The parasitic layer is composed of ~250 nm GaAs and ~40 nm InGaAs across the entire substrate surface. To remove the parasitic layer, the sample was covered with maP-1240 photoresist, to the NWs completely. E-beam lithography was used to expose and develop resist everywhere on the sample except in 2 μ m diameter circles around selected NWs. Wet etching using citric acid and hydrogen peroxide was used to etch all regions not protected by resist. The resist regions were then removed using acetone and isopropanol. The NWs were then shortened to a length of approximately 1.5 μ m by covering them partially with S1818 resist (approximately 1.5 μ m thick). Oxygen plasma was used to remove the thin resist layer on the top of the NWs. The NWs were then etched using HCl followed by citric acid and hydrogen peroxide. The resist layer was then removed with acetone and isopropanol.

µ-Photoluminescence measurements

Single NWs were excited at a temperature of 10 K using a pulsed titanium sapphire laser (excitation energy 1.59 eV, repetition rate 82 MHz, spot diameter 4 µm) and detected by a Horiba Triax 550 spectrometer with an LN2 cooled InGaAs array photodetector. The NWs were standing on their native growth substrate, where the excitation and detection were performed from the top.

BCDI measurements and reconstructions

An ASI Quad (512×512) Timpix detector with $55\times55 \,\mu\text{m}^2$ pixels was placed at 7.3° (γ) vertically and 22.9° (δ) horizontally at a distance of 1 m from the sample. Diffraction patterns were collected with a 20 second exposure at angular steps of 0.01° and an angular range between $1.5-2^{\circ}$ to collect

the majority of the 3D reciprocal space patterns. Six NWs were measured at the $(11\overline{1})$ condition and five of the same wires were measured at the $(1\overline{1}1)$ condition. Additionally, the (111) was measured on NW-2 in order to confirm the presence of twinning in the NWs.

3D reconstructions were obtained via an iterative phase retrieval algorithms in a Python module. ⁵⁶ The reconstruction process used in this work is well described in literature, ^{68,69} as are the error reduction algorithms. ^{70,71} Reconstructions were performed 10 times for each diffraction peak using different initial random guesses. 2D/3D reconstructions shown in this work are from single reconstructions, but strain quantified in line plots is averaged from the best four reconstructions (lowest pixel by pixel cross-correlations), with error given by the variations between reconstructions. Given there are two solutions to the BCDI phase retrieval problem: $\rho(r)$ and $\rho^*(-r)$, the solution that most closely resembled the asymmetry in the QW structure was used since the NWs were aligned in the beam with known orientation. Additionally, phase ramps were removed by centering the 3D diffraction patterns at the center voxel of the reconstruction grid.

Acknowledgment

M.O.H., C.H., and L.J.L. acknowledge the support of the National Science Foundation via DMR-1611341 and DMR 1905768. M.O.H. acknowledges support via the NSF GRFP. G.K, J.J.F., and P.S. acknowledge support from the Deutsche Forschungsgemeinschaft (DFG) via Project Grants FI 947/4-1 and KO 4005/7-1, the Cluster of Excellence e-conversion (EXC2089/1-390776260), and the European Research Council (ERC project QUANtIC, ID: 771747). Bragg CDI experiments and data processing were supported by the U.S. Department of Energy, Office of Science, Basic Energy Sciences, Materials Science and Engineering Division. CDI was performed at the Coherent Diffraction Imaging beamline 34-ID-C operated by the Advanced Photon Source at Argonne National Laboratory. This research used resources of the Advanced Photon Source, a U.S. Department of Energy (DOE) Office of Science user facility operated for the DOE Office of Science by Argonne National Laboratory under Contract No. DE-AC02-06CH11357. This work

made use of the EPIC facility of the NUANCE Center at Northwestern University, which has received support from the Soft and Hybrid Nanotechnology Experimental (SHyNE) Resource (NSF ECCS-1542205); the MRSEC program (NSF DMR-1720139) at the Materials Research Center; the International Institute for Nanotechnology (IIN); the Keck Foundation; and the State of Illinois, through the IIN. The authors are also grateful for assistance from W. Cha, M.J. Moody, Z. Zhu, and J. Olding in performing CDI measurements and M.O.H. would like to thank A. Davtyan for his useful discussions around experimental planning.

Author Contributions

M.O.H. and P.S. contributed equally to this work and co-wrote the manuscript. P.S. grew and processed the nanowire heterostructures. P.S. performed μ-PL measurements, analysis, and simulations. P.S. received guidance from G.K. and J.J.F. M.O.H. designed and performed BCDI measurements with the aid of S.O.H. and C.H. M.O.H. performed the COMSOL simulations, scattering simulations, and BCDI reconstructions. S.M. and S.O.H. aided in BCDI reconstructions and interpretation. C.H. performed TEM measurements and C.H. and X.H. performed STEM-EDX. M.O.H. and C.H. received guidance from L.J.L.

Supporting Information Available:

Details of NW growth and processing, power-dependent μ -PL measurement, PL simulation details, BCDI measurement details, BCDI reconstruction details, FEM and kinematic scattering simulation details, TEM and EDX analysis.

References

1. Svensson, C. P. T.; Mårtensson, T.; Trägårdh, J.; Larsson, C.; Rask, M.; Hessman, D.; Samuelson, L.; Ohlsson, J. Monolithic GaAs/InGaP Nanowire Light Emitting Diodes on Silicon.

- Nanotechnology 2008, 19, 305201.
- 2. Koblmüller, G.; Mayer, B.; Stettner, T.; Abstreiter, G.; Finley, J. J. GaAs–AlGaAs Core–Shell Nanowire Lasers on Silicon: Invited Review. *Semicond. Sci. Technol.* **2017**, *32*, 053001.
- 3. LaPierre, R. R.; Robson, M.; Azizur-Rahman, K. M.; Kuyanov, P. A Review of III–V Nanowire Infrared Photodetectors and Sensors. *J. Phys. D: Appl. Phys.* **2017**, *50*, 123001.
- 4. Lee, Y.-H.; Fu, L.; Li, Z.; Breuer, S.; Tan, H.; Jagadish, C.; Parkinson, P. Nanowire Solar Cells for Next-Generation Photovoltaics. *SPIE Newsroom* **2013**,
- 5. Tomioka, K.; Yoshimura, M.; Fukui, T. A III–V Nanowire Channel on Silicon for High-Performance Vertical Transistors. *Nature* **2012**, *488*, 189–192.
- Morkötter, S.; Jeon, N.; Rudolph, D.; Loitsch, B.; Spirkoska, D.; Hoffmann, E.; Döblinger, M.;
 Matich, S.; Finley, J. J.; Lauhon, L. J.; Abstreiter, G.; Koblmüller, G. Demonstration of Confined Electron Gas and Steep-Slope Behavior in Delta-Doped GaAs-AlGaAs Core-Shell Nanowire Transistors. *Nano Lett.* 2015, 15, 3295–3302.
- Mårtensson, T.; Svensson, C. P. T.; Wacaser, B. A.; Larsson, M. W.; Seifert, W.; Deppert, K.; Gustafsson, A.; Wallenberg, L. R.; Samuelson, L. Epitaxial III-V Nanowires on Silicon. *Nano Lett.* 2004, 4, 1987–1990.
- 8. Grönqvist, J.; Søndergaard, N.; Boxberg, F.; Guhr, T.; Åberg, S.; Xu, H. Q. Strain in Semiconductor Core-Shell Nanowires. *J. Appl. Phys.* **2009**, *106*, 053508.
- Nazarenko, M. V.; Sibirev, N. V.; Ng, K. W.; Ren, F.; Ko, W. S.; Dubrovskii, V. G.; Chang-Hasnain, C. Elastic Energy Relaxation and Critical Thickness for Plastic Deformation in the Core-Shell InGaAs/GaAs Nanopillars. *J. Appl. Phys.* 2013, 113, 104311.
- Salehzadeh, O.; Kavanagh, K. L.; Watkins, S. P. Geometric Limits of Coherent III-V Core/Shell Nanowires. J. Appl. Phys. 2013, 114, 054301.

- Dayeh, S. A.; Tang, W.; Boioli, F.; Kavanagh, K. L.; Zheng, H.; Wang, J.; Mack, N. H.;
 Swadener, G.; Huang, J. Y.; Miglio, L.; Tu, K.-N.; Picraux, S. T. Direct Measurement of
 Coherency Limits for Strain Relaxation in Heteroepitaxial Core/Shell Nanowires. *Nano Lett.* 2012, 13, 1869–1876.
- 12. Balaghi, L.; Shan, S.; Fotev, I.; Moebus, F.; Rana, R.; Venanzi, T.; Hübner, R.; Mikolajick, T.; Schneider, H.; Helm, M.; Pashkin, A.; Dimakis, E. High Electron Mobility in Strained GaAs-Nanowires. *Nat. Commun.* **2021**, *12*.
- 13. Schmiedeke, P.; Thurn, A.; Matich, S.; Döblinger, M.; Finley, J. J.; Koblmüller, G. Low-Threshold Strain-Compensated InGaAs/(In, Al)GaAs Multi-Quantum Well Nanowire Lasers Emitting Near 1.3 μm At Room Temperature. *Appl. Phys. Lett.* **2021**, *118*, 221103.
- Conesa-Boj, S.; Li, A.; Koelling, S.; Brauns, M.; Ridderbos, J.; Nguyen, T. T.; Verheijen, M. A.; Koenraad, P. M.; Zwanenburg, F. A.; Bakkers, E. P. A. M. Boosting Hole Mobility in Coherently Strained [110]-Oriented Ge–Si Core–Shell Nanowires. *Nano Lett.* 2017, 17, 2259–2264.

15.

- Yan, X.; Fan, S.; Zhang, X.; Ren, X. Analysis of Critical Dimensions for Nanowire Core-Multishell Heterostructures. *Nanoscale Res. Lett.* 2015, 10, 389.
- 17. Raychaudhuri, S.; Yu, E. T. Critical Dimensions in Coherently Strained Coaxial Nanowire Heterostructures. *J. Appl. Phys.* **2006**, *99*, 114308.
- Montazeri, M.; Fickenscher, M.; Smith, L. M.; Jackson, H. E.; Yarrison-Rice, J.; Kang, J. H.;
 Gao, Q.; Tan, H. H.; Jagadish, C.; Guo, Y.; Zou, J.; Pistol, M.-E.; Pryor, C. E. Direct Measure of Strain and Electronic Structure in GaAs/GaP Core-Shell Nanowires. *Nano Lett.* 2010, 10, 880–886.

- 19. Balaghi, L.; Bussone, G.; Grifone, R.; Hübner, R.; Grenzer, J.; Ghorbani-Asl, M.; Krashenin-nikov, A. V.; Schneider, H.; Helm, M.; Dimakis, E. Widely Tunable GaAs Bandgap Via Strain Engineering in Core/Shell Nanowires with Large Lattice Mismatch. *Nat. Commun.* **2019**, *10*.
- Keplinger, M.; Mårtensson, T.; Stangl, J.; Wintersberger, E.; Mandl, B.; Kriegner, D.; Holý, V.;
 Bauer, G.; Deppert, K.; Samuelson, L. Structural Investigations of Core-shell Nanowires Using
 Grazing Incidence X-ray Diffraction. *Nano Lett.* 2009, 9, 1877–1882.
- Grandal, J.; Wu, M.; Kong, X.; Hanke, M.; Dimakis, E.; Geelhaar, L.; Riechert, H.; Trampert, A. Plan-View Transmission Electron Microscopy Investigation of GaAs/(In, Ga)As Core-Shell Nanowires. *Appl. Phys. Lett.* 2014, 105, 121602.
- 22. Conesa-Boj, S.; Boioli, F.; Russo-Averchi, E.; Dunand, S.; Heiss, M.; Rüffer, D.; Wyrsch, N.; Ballif, C.; Miglio, L.; Fontcuberta i Morral, A. Plastic and Elastic Strain Fields in GaAs/Si Core–Shell Nanowires. *Nano Lett.* 2014, 14, 1859–1864.
- 23. Popovitz-Biro, R.; Kretinin, A.; Von Huth, P.; Shtrikman, H. InAs/GaAs Core–Shell Nanowires. *Cryst. Growth Des.* **2011**, *11*, 3858–3865.
- 24. Hassan, A. A.; Davtyan, A.; Küpers, H.; Lewis, R. B.; Bahrami, D.; Bertram, F.; Bussone, G.; Richter, C.; Geelhaar, L.; Pietsch, U. Complete Structural and Strain Analysis of Single GaAs/(In,Ga)As/GaAs Core–Shell–Shell Nanowires By Means of In-Plane and Out-of-Plane X-ray Nanodiffraction. *J. Appl. Crystallogr.* 2018, 51, 1387–1395.
- 25. Hassan, A. A.; Lähnemann, J.; Leake, S.; Küpers, H.; Niehle, M.; Bahrami, D.; Bertram, F.; Lewis, R. B.; Davtyan, A.; Schülli, T. U.; Geelhaar, L.; Pietsch, U. Spatially-Resolved Luminescence and Crystal Structure of Single Core—Shell Nanowires Measured in the As-Grown Geometry. *Nanotechnology* 2020, 31, 214002.
- 26. Dzhigaev, D.; Stankevič, T.; Bi, Z.; Lazarev, S.; Rose, M.; Shabalin, A.; Reinhardt, J.; Mikkelsen, A.; Samuelson, L.; Falkenberg, G.; Feidenhans'l, R.; Vartanyants, I. A. X-ray

- Bragg Ptychography on a Single InGaN/GaN Core–Shell Nanowire. *ACS Nano* **2017**, *11*, 6605–6611.
- 27. Davtyan, A.; Krause, T.; Kriegner, D.; Al-Hassan, A.; Bahrami, D.; Mostafavi Kashani, S. M.; Lewis, R. B.; Küpers, H.; Tahraoui, A.; Geelhaar, L.; Hanke, M.; Leake, S. J.; Loffeld, O.; Pietsch, U. Threefold Rotational Symmetry in Hexagonally Shaped Core–Shell (In,Ga)As/GaAs Nanowires Revealed By Coherent X-ray Diffraction Imaging. *J. Appl. Crystallogr.* 2017, 50, 673–680.
- Davtyan, A.; Biermanns, A.; Loffeld, O.; Pietsch, U. Determination of the Stacking Fault Density in Highly Defective Single GaAs Nanowires By Means of Coherent Diffraction Imaging.
 New J. Phys. 2016, 18, 063021.
- Favre-Nicolin, V.; Mastropietro, F.; Eymery, J.; Camacho, D.; Niquet, Y. M.; Borg, B. M.; Messing, M. E.; Wernersson, L.-E.; Algra, R. E.; Bakkers, E. P. A. M.; Metzger, T. H.; Harder, R.; Robinson, I. K. Analysis of Strain and Stacking Faults in Single Nanowires using Bragg Coherent Diffraction Imaging. New J. Phys. 2010, 12, 035013.
- 30. Chamard, V.; Stangl, J.; Labat, S.; Mandl, B.; Lechner, R. T.; Metzger, T. H. Evidence of Stacking-Fault Distribution Along an InAs Nanowire Using Micro-Focused Coherent X-ray Diffraction. *J. Appl. Crystallogr.* **2008**, *41*, 272–280.
- 31. Chamard, V.; Diaz, A.; Stangl, J.; Labat, S. Structural Investigation of InAs Nanowires with Coherent X-rays. *J. Strain Anal. Eng. Des.* **2009**, *44*, 533–542.
- 32. Shin, J.; Cornelius, T. W.; Labat, S.; Lauraux, F.; Richard, M.-I.; Richter, G.; Blanchard, N. P.; Gianola, D. S.; Thomas, O. In situ Bragg Coherent X-ray Diffraction During Tensile Testing of an Individual Au Nanowire. *J. Appl. Crystallogr.* **2018**, *51*, 781–788.
- 33. Gulden, J.; Mariager, S. O.; Mancuso, A. P.; Yefanov, O. M.; Baltser, J.; Krogstrup, P.; Patommel, J.; Burghammer, M.; Feidenhans'l, R.; Vartanyants, I. A. Coherent X-ray Nanodiffraction on Single GaAs Nanowires. *Phys. Status Solidi A* **2011**, *208*, 2495–2498.

- 34. Davydok, A.; Cornelius, T. W.; Ren, Z.; Leclere, C.; Chahine, G.; Schülli, T.; Lauraux, F.; Richter, G.; Thomas, O. In Situ Coherent X-ray Diffraction during Three-Point Bending of a Au Nanowire: Visualization and Quantification. *Quantum Beam Sci.* **2018**, *2*, 24.
- 35. Huang, X.; Harder, R.; Leake, S.; Clark, J.; Robinson, I. Three-dimensional Bragg Coherent Diffraction Imaging of an Extended ZnO Crystal. *J. Appl. Crystallogr.* **2012**, *45*, 778–784.
- 36. Kim, J. W.; Ulvestad, A.; Manna, S.; Harder, R.; Fullerton, E. E.; Shpyrko, O. G. 3D Bragg Coherent Diffractive Imaging of Five-Fold Multiply Twinned Gold Nanoparticle. *Nanoscale* **2017**, *9*, 13153–13158.
- Hofmann, F.; Phillips, N. W.; Harder, R. J.; Liu, W.; Clark, J. N.; Robinson, I. K.; Abbey, B. Micro-Beam Laue Alignment of Multi-Reflection Bragg Coherent Diffraction Imaging Measurements. *J. Synchrotron Radiat.* 2017, 24, 1048–1055.
- 38. Haag, S. T.; Richard, M.-I.; Labat, S.; Gailhanou, M.; Welzel, U.; Mittemeijer, E. J.; Thomas, O. Anomalous Coherent Diffraction of Core-Shell Nano-Objects: A Methodology for Determination of Composition and Strain Fields. *Phys. Rev. B* **2013**, *87*, 035408.
- 39. Diaz, A.; Mocuta, C.; Stangl, J.; Mandl, B.; David, C.; Vila-Comamala, J.; Chamard, V.; Metzger, T. H.; Bauer, G. Coherent Diffraction Imaging of a Single Epitaxial InAs Nanowire Using a Focused X-ray Beam. *Phys. Rev. B* 2009, 79, 125324.
- 40. Favre-Nicolin, V.; Eymery, J.; Koester, R.; Gentile, P. Coherent-Diffraction Imaging of Single Nanowires of Diameter 95 Nanometers. *Phys. Rev. B* **2009**, *79*, 195401.
- 41. Newton, M. C.; Sao, M.; Fujisawa, Y.; Onitsuka, R.; Kawaguchi, T.; Tokuda, K.; Sato, T.; Togashi, T.; Yabashi, M.; Ishikawa, T.; Ichitsubo, T.; Matsubara, E.; Tanaka, Y.; Nishino, Y. Time-Resolved Coherent Diffraction of Ultrafast Structural Dynamics in a Single Nanowire. *Nano Lett.* 2014, 14, 2413–2418.

- 42. Haag, S. T.; Richard, M. I.; Welzel, U.; Favre-Nicolin, V.; Balmes, O.; Richter, G.; Mittemeijer, E. J.; Thomas, O. Concentration and Strain Fields inside a Ag/Au Core–Shell Nanowire Studied by Coherent X-ray Diffraction. *Nano Lett.* **2013**, *13*, 1883–1889.
- 43. Davtyan, A.; Favre-Nicolin, V.; Lewis, R. B.; Küpers, H.; Geelhaar, L.; Kriegner, D.; Bahrami, D.; Al-Hassan, A.; Chahine, G.; Loffeld, O.; Pietsch, U. Coherent X-ray Diffraction Imaging Meets Ptychography to Study Core-Shell-Shell Nanowires. *MRS Adv.* **2018**, *3*, 2317–2322.
- 44. Labat, S.; Richard, M.-I.; Dupraz, M.; Gailhanou, M.; Beutier, G.; Verdier, M.; Mastropietro, F.; Cornelius, T. W.; Schülli, T. U.; Eymery, J.; Thomas, O. Inversion Domain Boundaries in GaN Wires Revealed By Coherent Bragg Imaging. *ACS Nano* **2015**, *9*, 9210–9216.
- 45. Spirkoska, D.; Arbiol, J.; Gustafsson, A.; Conesa-Boj, S.; Glas, F.; Zardo, I.; Heigoldt, M.; Gass, M. H.; Bleloch, A. L.; Estrade, S.; Kaniber, M.; Rossler, J.; Peiro, F.; Morante, J. R.; Abstreiter, G.; Samuelson, L.; i Morral, A. F. Structural and Optical Properties of High Quality Zinc-Blende/Wurtzite GaAs Nanowire Heterostructures. *Phys. Rev. B* 2009, 80, 245325.
- 46. Hill, M. O.; Calvo-Almazan, I.; Allain, M.; Holt, M. V.; Ulvestad, A.; Treu, J.; Koblmüller, G.; Huang, C.; Huang, X.; Yan, H.; Nazaretski, E.; Chu, Y. S.; Stephenson, G. B.; Chamard, V.; Lauhon, L. J.; Hruszkewycz, S. O. Measuring Three-Dimensional Strain and Structural Defects in a Single InGaAs Nanowire Using Coherent X-ray Multiangle Bragg Projection Ptychography. *Nano Lett.* 2018, 18, 811–819.
- 47. Anderson, N. G.; Laidig, W. D.; Kolbas, R. M.; Lo, Y. C. Optical Characterization of Pseudomorphic In_xGa_{1-x}As–GaAs Single-Quantum-Well Heterostructures. *J. Appl. Phys.* **1986**, *60*, 2361–2367.
- 48. Gal, M.; Taylor, P. C.; Usher, B. F.; Orders, P. J. Photoluminescence in Strained InGaAs-GaAs Heterostructures. *J. Appl. Phys.* **1987**, *62*, 3898–3901.

- 49. Grundmann, M.; Bimberg, D.; Fischer-Colbrie, A.; Miller, J. Recombination Dynamics in Pseudomorphic and Partially relaxed In 0.23 Ga 0.77 As/GaAs Quantum Wells. *Phys. Rev. B* **1990**, *41*, 10120.
- 50. Amand, T.; Marie, X.; Dareys, B.; Barrau, J.; Brousseau, M.; Dunstan, D.; Emery, J.; Goldstein, L. Well-Width Dependence of the Excitonic Lifetime in Strained III-V Quantum Wells. *J. appl. Phys.* **1992**, *72*, 2077–2079.
- 51. Yu, H.; Roberts, C.; Murray, R. Influence of Indium Segregation on the Emission from In-GaAs/GaAs Quantum Wells. *Appl. Phys. Lett.* **1995**, *66*, 2253–2255.
- 52. Birner, S.; Zibold, T.; Andlauer, T.; Kubis, T.; Sabathil, M.; Trellakis, A.; Vogl, P. nextnano: General Purpose 3-D Simulations. *IEEE Trans. Electron Devices* **2007**, *54*, 2137–2142.
- 53. Rossi, F.; Molinari, E. Coulomb-Induced Suppression of Band-Edge Singularities in the Optical Spectra of Realistic Quantum-Wire Structures. *Phys. Rev. Lett.* **1996**, *76*, 3642–3645.
- 54. Miao, J.; Kirz, J.; Sayre, D. The Oversampling Phasing Method. *Acta Crystallogr., Sect. D: Biol. Crystallogr.* **2000**, *56*, 1312–1315.
- 55. Rudolph, D.; Schweickert, L.; Morkötter, S.; Hanschke, L.; Hertenberger, S.; Bichler, M.; Koblmüller, G.; Abstreiter, G.; Finley, J. J. Probing the Trapping and Thermal Activation Dynamics of Excitons at Single Twin Defects in GaAs–AlGaAs Core–Shell Nanowires. *New J. Phys.* 2013, 15, 113032.
- 56. Maddali, S. Phaser: Python-Based BCDI Phase Retrieval for CPU and GPU. 2020.
- 57. Ulvestad, A.; Menickelly, M.; Wild, S. M. Accurate, Rapid Identification of Dislocation Lines in Coherent Diffractive Imaging Via a Min-Max Optimization Formulation. *AIP Adv.* **2018**, 8, 015114.
- 58. Shi, X.; Clark, J. N.; Xiong, G.; Huang, X.; Harder, R.; Robinson, I. K. Mechanical Breakdown

- of Bent Silicon Nanowires Imaged by Coherent X-ray Diffraction. *New J. Phys.* **2013**, *15*, 123007.
- 59. Ulvestad, A.; Clark, J. N.; Harder, R.; Robinson, I. K.; Shpyrko, O. G. 3D Imaging of Twin Domain Defects in Gold Nanoparticles. *Nano Lett.* **2015**, *15*, 4066–4070.
- 60. Liu, Y.; Lopes, P. P.; Cha, W.; Harder, R.; Maser, J.; Maxey, E.; Highland, M. J.; Markovic, N. M.; Hruszkewycz, S. O.; Stephenson, G. B. Stability Limits and Defect Dynamics in Ag Nanoparticles Probed By Bragg Coherent Diffractive Imaging. *Nano Lett.* 2017, 17, 1595–1601.
- 61. Glas, F. Strain in Nanowires and Nanowire Heterostructures. *Semicond. Semimetals* **2015**, *93*, 79–123.
- 62. Wang, S. Lattice Engineering: Technology and Applications; CRC Press, 2012.
- 63. Trushin, O.; Granato, E.; Ying, S. C.; Salo, P.; Ala-Nissila, T. Energetics and atomic mechanisms of dislocation nucleation in strained epitaxial layers. *Physical Review B* **2003**, *68*, 155413.
- 64. Elman, B.; Koteles, E. S.; Melman, P.; Ostreicher, K.; Sung, C. Low Substrate Temperature Molecular Beam Epitaxial Growth and the Critical Layer Thickness of InGaAs Grown on GaAs. *J. Appl. Phys.* **1991**, *70*, 2634–2640.
- 65. Caroff, P.; Dick, K. A.; Johansson, J.; Messing, M. E.; Deppert, K.; Samuelson, L. Controlled Polytypic and Twin-Plane Superlattices in III-V Nanowires. *Nat. Nanotechnol.* **2009**, *4*, 50–55.
- 66. Jeon, N.; Ruhstorfer, D.; Döblinger, M.; Matich, S.; Loitsch, B.; Koblmüller, G.; Lauhon, L. Connecting Composition-Driven Faceting with Facet-Driven Composition Modulation in GaAs–AlGaAs Core–Shell Nanowires. *Nano Lett.* 2018, 18, 5179–5185.
- 67. Stettner, T.; Thurn, A.; Döblinger, M.; Hill, M. O.; Bissinger, J.; Schmiedeke, P.; Matich, S.; Kostenbader, T.; Ruhstorfer, D.; Riedl, H.; Kaniber, M.; Lauhon, L. J.; Finley, J. J.;

- Koblmüller, G. Tuning Lasing Emission Toward Long Wavelengths in GaAs-(In, Al)GaAs Core–Multishell Nanowires. *Nano Lett.* **2018**, *18*, 6292–6300.
- 68. Maddali, S.; Li, P.; Pateras, A.; Timbie, D.; Delegan, N.; Crook, A. L.; Lee, H.; Calvo-Almazan, I.; Sheyfer, D.; Cha, W.; Heremans, F. J.; Awschalom, D. D.; Chamard, V.; Allain, M.; Hruszkewycz, S. O. General Approaches for Shear-Correcting Coordinate Transformations in Bragg Coherent Diffraction Imaging. Part I. J. Appl. Crystallogr. 2020, 53, 393–403.
- Li, P.; Maddali, S.; Pateras, A.; Calvo-Almazan, I.; Hruszkewycz, S. O.; Cha, W.; Chamard, V.;
 Allain, M. General Approaches for Shear-Correcting Coordinate Transformations in Bragg
 Coherent Diffraction Imaging. Part II. J. Appl. Crystallogr. 2020, 53, 404–418.
- 70. Fienup, J. R. Phase Retrieval Algorithms: a Comparison. Appl. Opt. 1982, 21, 2758–2769.
- 71. Fienup, J. R. Phase Retrieval Algorithms: a Personal Tour [Invited]. *Appl. Opt.* **2013**, *52*, 45–56.